Article

Journal of the Brazilian Chemical Society

https://dx.doi.org/10.21577/0103-5053.20240126

J. Braz. Chem. Soc. **2024**, *35*, 12, e-20240126, 1-11

Exploring Iron Oxide Catalysts for Acetone Hydrodeoxygenation: Making Use of an Earth-Abundant Resource

Pedro B. M. Nunes,[#,a] *Guilherme B. Strapasson,*[#,a,b] *Gabriel B. Báfero*[#,a] *and Daniela Zanchet*[*,a]

[a]*Instituto de Química, Universidade de Campinas (UNICAMP), 13083-970 Campinas-SP, Brazil*

[b]*Laboratório Nacional de Luz Síncrotron, CNPEM, 13083-100 Campinas-SP, Brazil*

The catalytic performance of γ-Fe_2O_3 nanopowder was investigated in the acetone hydrodeoxygenation (HDO) reaction, an essential catalytic reaction in biomass valorization. Sequential reduction/oxidation thermal pre-treatments of the γ-Fe_2O_3 nanopowder induced significant structural and electronic modifications that directly impacted its catalytic performance. The co-existence of Fe^{3+}/Fe^{2+}/Fe^0 sites led to different reaction pathways (C–C coupling, hydrogenolysis, hydrogenation, and (hydro)deoxygenation) that formed a wide range of products. The correlation of the catalytic and structural data provided a better understanding of C–O, C–C, and C–H bond activation under the HDO reactional stream in the presence of metallic and oxidized phases of iron. This study demonstrates the tunability of FeO_x catalysts in the acetone HDO reaction to favor different reaction pathways and the formation of products. It highlights that tailoring active sites is crucial for developing selective and optimized catalysts for the HDO reaction.

Keywords: heterogeneous catalysis, iron oxide, hydrodeoxygenation reaction

Introduction

The escalating demand for energy and the pressing global warming issues are driving constant innovations in converting greenhouse gases and renewable feedstocks into valuable fuels and chemicals. In this sense, biomass has gained space both in research and industry; beyond its non-fossil origin, biomass stands out as an abundant and chemically rich raw material.[1] The hydrodeoxygenation (HDO) reaction is one of the main biomass-derivatives upgrading processes to produce biofuels, in which lignocellulosic bio-oils can be employed as raw materials.[1] These bio-oils are complex mixtures of oxygenated compounds, ranging from ketones and aldehydes to carboxylic acids and sugars.[2] The HDO reaction aims to reduce the oxygen content of these compounds by selectively cleaving C–O bonds under H_2 atmosphere in the presence of a solid catalyst. Nevertheless, other sequential and parallel steps take place beside the C–O cleavage, which can lead to a complex reaction network, and representative model molecules, such as acetone, have been used to help identify the catalytic sites and the most favored pathways.[3] Scheme 1 shows a general reaction network for the acetone HDO reaction, exhibiting the main products and the catalytic sites through which they can be obtained: Lewis and Brønsted acid sites (AS), oxygen vacancy sites (OVS), and metallic sites (MS).

Concerning the catalysts, due to the high cost, low availability, and susceptible deactivation of noble metals, catalysts based on earth-abundant elements have aroused interest as promising and affordable candidates for the HDO reaction.[4] Among the transition metals, iron is the most abundant element in Earth's crust, corresponding to 5.6% of all elements and 88.6% of the transition metals.[5] Table 1 depicts the crystallographic properties and structures of metallic and most common oxidized phases of iron.

Iron-based catalysts stand out as remarkably versatile materials, playing a pivotal role in numerous crucial industrial chemical processes[8-10] and emerging applications.[11,12] When considered as a catalyst for HDO, iron exhibits more favorable attributes compared to neighboring metals (i.e., Co, Ni, and Cu),[13] particularly in the production of deoxygenated aromatics from phenols (anisole, guaiacol, cresol) and other benzyl compounds. Iron hydrogenation capability is insufficient to completely

*e-mail: zanchet@unicamp.br
Editor handled this article: Aldo José Gorgatti Zarbin (Guest)
[#]These authors contributed equally.
We dedicate this article as a tribute to the legacy and scientific enthusiasm of Prof Oswaldo L. Alves.

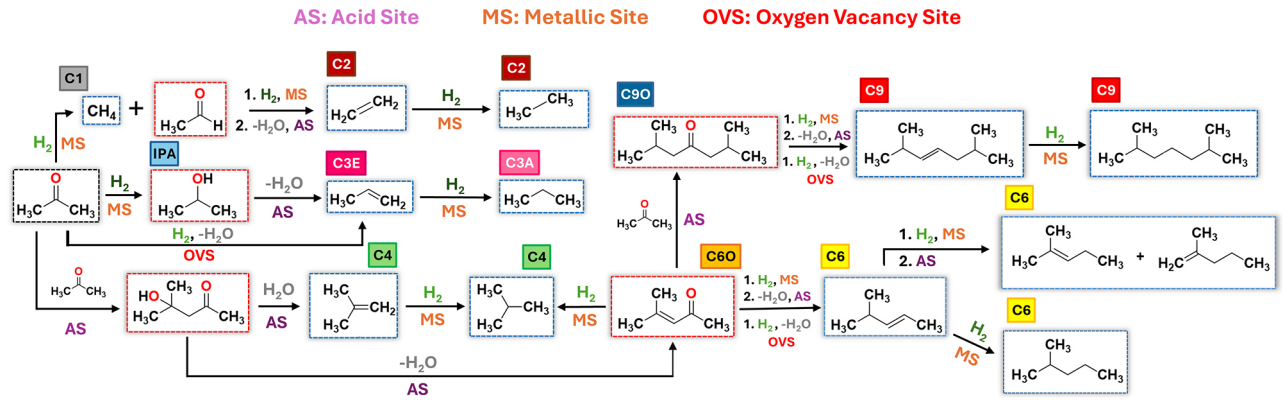

Scheme 1. Reaction scheme for acetone HDO for FeO_x catalysts. Deoxygenated products are highlighted in gray, and abbreviations for each main product are in black (minor characters) (adapted from Leite *et al.*[3]).

Table 1. Structural features of metallic Fe and FeO, Fe_3O_4, α- and γ-Fe_2O_3. Data was collected from the Inorganic Crystal Structure Database (ICSD)[6] and constructed using VESTA.[7] The shortest bond distances were taken into consideration

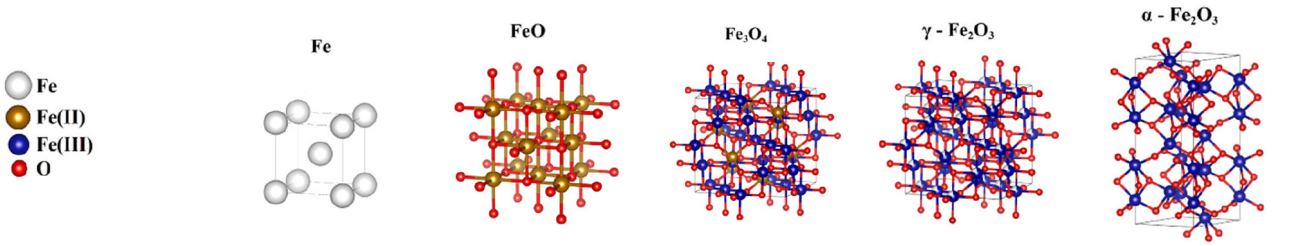

	Fe	FeO	Fe_3O_4	γ - Fe_2O_3	α - Fe_2O_3
ICSD collCode	48382	82233	20596	247034	71194
Structure type	bcc	NaCl	inverse spinel	defect spinel	corundum
Iron site	Fe^0 at cubic site	Fe^{2+} at O_h	Fe^{2+} at T_d Fe^{3+} at O_h	Fe^{3+} at T_d and O_h	Fe^{3+} at O_h
Fe–Fe distance / Å	2.48	3.06[a]	3.64[a] 2.97[b] 3.48[c]	2.96	2.97
O–O distance / Å	–	3.06	2.78	2.96	3.03
Fe–O distance / Å	–	2.16	1.93[d] 2.03[e]	1.90	1.94
Lattice parameter / Å	2.86	4.33	8.40	8.37	a = 5.04 b = 5.04 c = 13.76
No. of sites *per* unit cell	2 Fe^0	4 Fe^{2+}, 4 O^{2-}	8 Fe^{2+},16 Fe^{3+}, 32 O^{2-}	24 ⅓ Fe^{3+}, 32 O^{2-}	12 Fe^{3+}, 18 O^{2-}

[a]Fe^{2+}–Fe^{2+}; [b] Fe^{3+}–Fe^{3+}; [c]Fe^{3+}–Fe^{2+}; [d]Fe^{2+}–O; [e]Fe^{3+}–O. O_h: octahedral site, T_d: tetrahedral site.

hydrogenate aromatics such as benzene, distinguishing it from metals such as Ni, Pd, Pt, Co, or Cu.[4] This makes Fe-based catalysts advantageous for the HDO of phenolics by selectively yielding deoxygenated aromatics with a higher octane rating. As an oxophilic transition metal, iron tends to interact with the carbonyl group rather than engage in aromatic ring hydrogenation, resulting in selective C–O bond cleavage products.[4] Nevertheless, challenges persist in the form of diminished activity and catalyst deactivation, attributed to carbon deposition and Fe-oxidation in the presence of water.[13]

Many different Fe-based catalysts have been studied for the HDO reaction: supported on alumina,[14,15] silica,[16-18] ceria,[19,20] zirconia,[21] magnesium aluminate,[22] and carbon matrices;[16,23,24] in the form of carbides,[25,26] phosphides,[27] and sulfides;[28] as part of bimetallic structures[29,30] or graphene composites.[31] However, few HDO studies were dedicated to pure iron/iron oxide phases as bulk catalysts. Prasomsri *et al.*[32] screened several transition-metal oxides (iron oxide included) using acetone HDO. The γ-Fe_2O_3 phase showed good acetone conversion and deoxygenation degree at 400 ºC, presumably promoted by the reverse

Mars-van Krevelen mechanism through the oxygen vacancies generated under reaction conditions.[32] This interpretation was based on the well-known activity of γ-Fe_2O_3 in oxidation reactions through the direct Mars-van Krevelen mechanism.[33]

The phase transition or coexistence of metallic and oxidized phases of iron (i.e., Fe^0, FeO, Fe_3O_4, α- and γ-Fe_2O_3) under HDO reactional stream leads to different active sites (e.g., metallic, acid, and redox) that can catalyze different reaction pathways, as shown in Scheme 1.[3,34,35] Metallic and acid sites can be combined in a bifunctional mechanism, with H_2 being activated in the former and the C–O bond cleavage being caused by the latter, in a dehydration step.[36] These mechanisms may also occur separately, with metal-catalyzed hydrogenations/hydrogenolysis and Brønsted/Lewis acid aldol condensations taking place independently. Lastly, the direct deoxygenation route via the reverse Mars-van Krevelen mechanism, in which the oxygen vacancies are the active sites, can also be favored. Previous reports[37-40] on iron and other metal oxide catalysts demonstrated that Lewis-type cationic $M^{\delta+}$ sites, related to oxygen vacancies, and Brønsted acid sites, as surface M–OH groups, can be generated over the surface. Iron metallic sites can also be formed under a reducing atmosphere at high temperatures.

Leite *et al.*[3] demonstrated that reducing/oxidizing thermal pre-treatments can achieve different phases and catalytic sites over reducible metal oxides. They investigated the tuning of the $Co^0/Co^{2+}/Co^{3+}$ ratio in bulk Co-based catalysts, leading to an enhancement of the C–O/C–C bond cleavages ratio over acetone HDO. Here, we focused on evaluating FeO_x systems and their catalytic properties in the acetone HDO. Sequential reduction/oxidation pre-treatments were applied to the γ-Fe_2O_3 nanopowder as a function of temperature to induce structural and electronic modifications. Investigating acetone HDO not only has direct relevance to biomass-derivatives upgrading but also provides valuable means to probe the catalyst properties of FeO_x catalysts and to understand the role of catalytic sites in activating and cleaving C–O, C–C, and C–H bonds.[3,32,34,35] The structural properties of the catalysts were also characterized to gain further insights, allowing better correlations with the catalytic data and reaction pathways.

Experimental

Materials

Gamma iron(III) oxide (γ-Fe_2O_3, nanopowder, < 50 nm mean particle size), aluminum oxide (α-Al_2O_3, 99%, 100 mesh), acetone (≥ 99.9%, HPLC Plus Grade), and pyridine (anhydrous, 99.8%), were purchased from Sigma-Aldrich (Saint Louis, USA).

Reducing and oxidizing thermal pre-treatments

The reduction pre-treatment of the γ-Fe_2O_3 nanopowder was conducted at 550 ºC for 1 h, employing 30% H_2 in He with a total flow of 100 mL min^{-1}. Calcination pre-treatments were conducted over the reduced catalyst at different temperatures (200, 350, and 500 ºC), for 2 h, using synthetic air (50 mL min^{-1}). The catalysts were labeled according to the pre-treatments, e.g., Red 550 stands for reduction at 550 ºC; while RedOxi X (X = 200, 350, or 500) stands for Red 550 oxidized at different temperatures, with X associated with the oxidation temperature. A passivation step was conducted for the *ex situ* characterization of the Red 550 catalyst, employing O_2 (2 mL min^{-1}) for 20 min.

Catalytic evaluation

Thermal pre-treatments under reducing and oxidizing atmospheres and the acetone HDO reaction were conducted in a fix-bed reactor equipped with a quartz bulb tube. Acetone was fed into the reactor using a saturator flask at a thermostatic bath at 10 ºC, with 20 mL min^{-1} of He carrying 3.6 mL min^{-1} of acetone. Hydrogen was also fed to the stream (76.4 mL min^{-1}), with a total flow of 100 mL min^{-1} (21 mol of H_2 *per* mol of acetone). The catalytic tests were performed as a function of temperature (100-400 ºC, with 100 ºC steps, 30 min at each temperature) or as a function of time on stream (TOS), at 300 or 400 ºC, for 3 h. 0.6 g of catalyst were employed for each test, with a weight hourly space velocity (WHSV, equation 1) of 0.94 h^{-1}.

$$\text{WHSV} = \frac{\text{Acetone mass feed rate (g h}^{-1})}{\text{Catalyst mass (g)}} \quad (1)$$

Products were analyzed by an on-line gas chromatograph (GC, Agilent Technologies, model 7890A, Wilmington, USA) equipped with a HP-1 column (50 m × 0.32 mm internal diameter, 0.17 μm). Major products and abbreviations were: methane (C1), ethane/ethylene (C2), propylene (C3E), propane (C3A), butane and isomers (C4), isopropanol (IPA), hexane/hexene and other open-chained isomers (C6), nonane/nonene and isomers (C9), mesityl oxide (C6O), 2,6-dimethyl-4-heptanone and isomers (C9O). All carbon balances obtained were higher than 0.85.

Acetone conversion and products distribution were calculated using equations 2 and 3, respectively, and the

deoxygenation degree (DD) using equation 4.

$$\text{Acetone conversion (\%)} = 100 \times \frac{\text{moles of acetone consumed}}{\text{moles of acetone fed}} \quad (2)$$

$$\text{Products distribution (\%)} = 100 \times \frac{\text{produced moles of the product}}{\text{moles of acetone consumed}} \quad (3)$$

DD (%) = sum of deoxygenated products (C1, C2, C3E/A, C4, C6 and C9) (4)

Characterization of the catalysts

Temperature programmed reduction using H_2 (TPR) measurements were performed in a triple filter quadrupole HPR-20 Hiden Analytical Mass Spectrometer (Warrington, England) to detect hydrogen consumption as a function of temperature. 200 mg of sample were treated under He flow (100 mL min^{-1}) at 200 ºC for 1 h, followed by the TPR measurement conducted under a 10% H_2/He atmosphere (total flow of 30 mL min^{-1}), with a 10 ºC min^{-1} temperature ramp up to 800 ºC.

X-ray diffraction (XRD) data were obtained in a D2 Phaser Bruker diffractometer (Karlsruhe, Germany), with Cu Kα radiation (1.5418 Å), with 2θ values ranging from 20 to 70º, at a step of 0.1º, 1.5º min^{-1}. Scherrer's equation was employed to determine the mean crystallite size.

N_2-physisorption was employed to measure the specific surface area (SSA) of the catalysts using a Quantachrome NOVA 4200e equipment (Boynton Beach, USA), and Brunauer-Emmett-Teller (BET) theory was used. Samples were degassed at 120 ºC for 24 h before analysis.

The acid sites concentration was determined using NH_3 temperature-programmed desorption (NH_3-TPD). Initially, a mass of 150 mg of sample was treated with He (60 mL min^{-1}) at 200 ºC for 1 h, followed by cooling down to 100 ºC. Subsequently, the sample was exposed to a 1% NH_3 in He flow (60 mL min^{-1}) for another 1 h at this temperature, saturating the surface. The physisorbed NH_3 was then removed under He flow for 1 h, and the temperature was raised to 400 ºC (10 ºC min^{-1}). Mass spectrometry was employed to analyze the NH_3 concentration in the effluent using a OmniStar Balzers Instrument (Leidschendam, Netherlands).

Attenuated total reflection Fourier transform infrared spectroscopy (ATR-FTIR) of adsorbed pyridine (Py) was used to measure the nature of the surface acid sites. Py-FTIR spectra were obtained using an Agilent Cary 660 spectrometer (Wilmington, USA) in the range 1700-1400 cm^{-1} with a resolution of 4 cm^{-1}; 64 scans were collected for signal accumulation. The adsorption of Py was done over the sample in powder form, which was previously dried at 150 ºC in vacuum (1 h) and N_2 flow (1 h), aiming for the desorption of impurities on the surface. N_2 carrying Py vapor was introduced into the flask with the pretreated catalyst kept at 120 ºC by a cannula connecting a liquid Py flask at 50 ºC for 1 h. Finally, the catalyst was purged with N_2 at 120 ºC for 1 h to remove the physisorbed Py. The final spectrum was obtained by subtracting the Py-adsorbed catalyst spectrum from the untreated one. Pyridine coordinatively bonds to Lewis acid sites resulting in bands around 1442 and 1605 cm^{-1}, while pyridinium ion, formed due to the interaction with Brønsted acid sites, shows bands around 1543 and 1646 cm^{-1}. The band at 1476 cm^{-1} is attributed to both coordinatively-bonded pyridine and pyridinium ion stretching vibrations.[41] The Brønsted/Lewis acid sites' ratio was determined by integrating the bands at 1442 and 1543 cm^{-1}, employing molar extinction coefficients of 1.73 and 1.23 cm $mmol^{-1}$ for Lewis and Brønsted acid sites, respectively.[41]

Results and Discussion

The as-received γ-Fe_2O_3 nanopowder catalyst was formed by interconnected particles (< 50 nm), with a SSA of 98 m^2 g^{-1} being tested in the acetone HDO reaction. The main expected reaction pathways and products were shown in Scheme 1, associated with different catalytic sites (AS, OVS, and MS). Figure 1a shows the catalytic performance as a function of temperature. At temperatures ≤ 200 ºC, low conversions of acetone (≤ 10%) were achieved and the formation of condensation products was favored (100%), demonstrating the predominance of AS. Acetone conversion increased to 26% at 300 ºC, with IPA representing about 6% of the total products and condensation products representing about 94%. At 400 ºC, the acetone conversion reached 42%, along with a higher hydrogenating capability, in which deoxygenated products represented 77% of the total products (9% to C1, 3% to C2, 23% to C3E, 20% to C3A, 7% to C4, and 14% to C6.

The as-received γ-Fe_2O_3 nanopowder catalyst was also evaluated in the acetone HDO reaction as a function of TOS at 300 ºC (Figure 1b) and 400 ºC (Figure 1c). At 300 ºC, the catalytic performance remained stable for 3 h on stream, with acetone conversions around 25%, and products distribution (averages) of C6O (78%), IPA (11%), C9O (7%), C4 (2%), C3E (1.3%), and C3A (0.7%). Similar to what was observed in Figure 1a, condensation products were favored. On the other hand, at 400 ºC the catalyst suffered a quick deactivation over TOS, with acetone conversions of 42% at the beginning of the reaction, going down to 16% after 3 h on stream. The deactivation of the catalyst was followed by changes in the products'

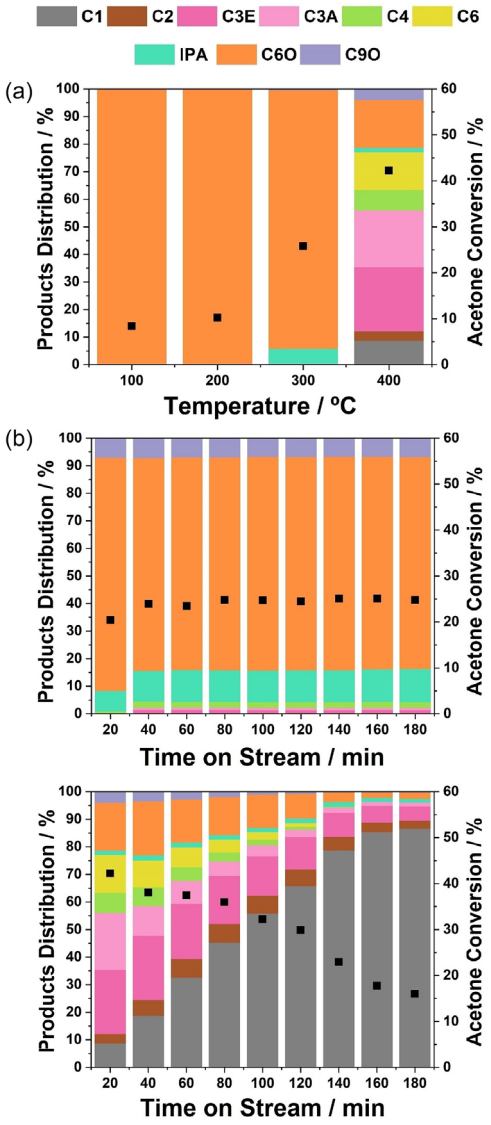

Figure 1. Product distribution (bars, left axis) and acetone conversions (squares, right axis) for the acetone HDO reaction using the as-received catalyst (a) as a function of temperature from 100 to 400 ºC, (b) as a function of TOS at 300 ºC, and (c) as a function of TOS at 400 ºC. Feed: 3.6 mL min^{-1} acetone, 76 mL min^{-1} H_2, balance He. 100 mL min^{-1} total flow. WHSV = 0.94 $g_{acetone}$ $[g_{iron}\ h]^{-1}$.

distribution, with an increase in methane over TOS. Acetone conversions and products' distribution of the first and last points of the reactions as a function of TOS are described in Table 2.

XRD measurements of the pre- and post-reaction catalysts are shown in Figure 2. The as-received γ-Fe_2O_3 nanopowder XRD pattern matches the maghemite phase, presenting a cubic crystal structure. A mean crystallite size of 20.7 nm was calculated considering the (311) reflection, corroborating the expected nanosized crystalline domains. The XRD patterns of the post-reaction catalyst of the 300 ºC isotherm (AR-HDO 300) presented an increase of 37% in the mean crystallite size after 3 h on stream (28.3 nm). In comparison, for the 400 ºC isotherm (AR-HDO 400), γ-Fe_2O_3/Fe_3O_4, and Fe_3C (ICSD collCode 99003) crystalline contributions were observed after 3 h on stream. Both γ-Fe_2O_3 and Fe_3O_4 phases present a cubic crystal structure with slight differences in the lattice parameter and were not attempted to be distinguished here (Table 1). The co-existence of multiple crystalline phases of iron demonstrates that the reactional environment led to major modifications of the catalyst at 400 ºC. The carburation of Fe-based catalysts into iron carbides (e.g., Fe_3C, Fe_5C_2) is a well-reported transformation under simultaneous reducing and carburizing atmospheres.[42,43] More detailed information on the mean crystallite sizes of the pre- and post-reaction catalysts is displayed in Table S1 (Supplementary Information (SI) section).

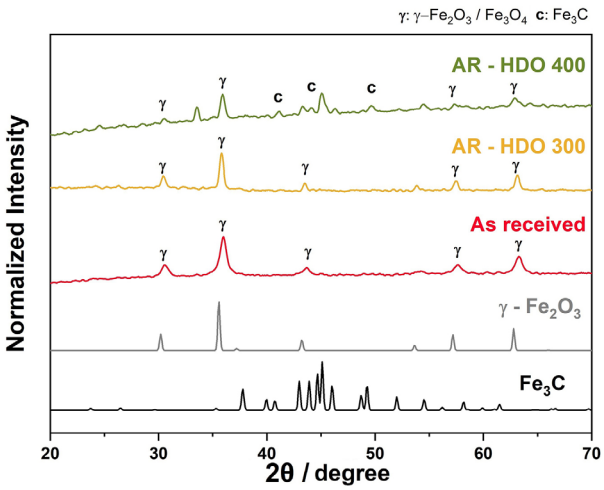

Figure 2. XRD patterns of the as-received γ-Fe_2O_3 nanopowder and post-reaction isotherms, at 300 ºC (AR-HDO 300) and 400 ºC (AR-HDO 400), after 3 h on stream. The theoretical XRD pattern of γ-Fe_2O_3 and Fe_3C phases are shown for comparison purposes.

Table 2. Initial (TOS = 20 min) and final (TOS = 180 min, within parenthesis) distribution of products, acetone conversions, and DD of the as-received γ-Fe_2O_3 nanopowder as a function of TOS at 300 and 400 ºC

Isotherm	Conversion / %	C1, C2, C4 / %	C3E/A / %	C6, C9 / %	IPA / %	C6O, C9O / %	DD / %
300 ºC	20.4 (24.7)	0.9 (2.1)	0.0 (2.3)	0.0 (0.0)	7.5 (11.9)	91.6 (83.6)	0.9 (4.5)
400 ºC	42.2 (16.0)	19.5 (89.7)	43.9 (6.5)	13.8 (0.0)	1.5 (1.4)	21.2 (2.5)	77.2 (96.2)

DD: deoxygenation degree; IPA: isopropanol.

The highly reducing atmosphere of the HDO reaction led to the partial reduction of the γ-Fe_2O_3 nanopowder to more reduced oxidic and carbidic phases. H_2-TPR of the as received γ-Fe_2O_3 nanopowder is shown in Figure S1 (SI section). The H_2-TPR profile presented two main H_2 consumption events: at 330 ºC, a first reduction associated with the transformation of γ-Fe_2O_3 to Fe_3O_4 occurred; at around 450 ºC, a second reduction step started, showing a maximum H_2 consumption at 630 ºC, associated with the formation of Fe^0.[44] The acetone HDO reactional atmosphere provided, in fact, a more reducing atmosphere (76% H_2 v/v) in comparison with the one used during the H_2-TPR measurement (10% H_2 v/v), facilitating the reduction of the oxidic iron phase at lower temperatures.

The acidic properties of the as-received γ-Fe_2O_3 nanopowder were probed by NH_3-TPD and Py-FTIR, shown in Figure 3. Both are considered classic techniques and employ basic molecules as probes to indirectly determine the AS concentration, nature, and strength.[45] NH_3-TPD assesses the overall AS concentration and strength but cannot distinguish between between Brønsted and Lewis acid sites (BAS and LAS). On the other hand, it is possible to distinguish BAS and LAS sites using Py-FTIR, as they present different absorption bands.

The NH_3-TPD profile (Figure 3a) shows AS with different strengths for the as-received γ-Fe_2O_3 sample. At least four distinct desorption regions (with maxima at 162, 223, 264, and 360 ºC) could be distinguished, indicating weak to moderate AS, with a total amount of AS of 80 μmol g^{-1}. This value is comparable to other quantifications reported by the literature. In a comprehensive study, Kayo *et al.*[46] prepared and characterized bulk γ-Fe_2O_3 using different synthetic routes. The AS concentrations found through NH_3-TPD ranged from 29 to 136 μmol g^{-1}, showing an expected correlation with the samples' SSA.[46]

The Py-FTIR spectrum (Figure 3b) shows two bands, at ca. 1543 and ca. 1442 cm^{-1}, that can be attributed to pyridine adsorbed at BAS and LAS, respectively, whereas the additional band at ca. 1476 cm^{-1} has contributions from both AS types.[41,47] It is well known that most reducible metal oxides, like γ-Fe_2O_3, can present Lewis-type cationic $M^{\delta+}$ sites, associated with structural defects (mostly related to oxygen vacancies), and surface M–OH species that give rise to BAS. The BAS/LAS ratio was around 1.2.

The catalytic performance of the as-received γ-Fe_2O_3 catalyst in the acetone HDO reaction (Figure 1 and Table 2) demonstrated that at temperatures ≤ 300 ºC condensation products were favored. The formation of these products was associated with the presence of AS in the γ-Fe_2O_3 surface. At 400 ºC, the catalyst presented a higher hydrogenating capability, leading to the formation of C–O direct bond cleavage products (C3E, C3A, C6 and C9; initially 57.7%, 6.5% at the end of TOS) and C–C bond cleavage products (C1, C2 and C4; starting at 19.5% and reaching 89.7% by the end of TOS), along with condensation products (C6O and C9O; from 21.2 to 2.5%). The change in selectivity suggests that more hydrogenating active sites were generated under reactional stream, confirmed through the formation of a carbidic iron phase (Figure 2), which presents a metallic behavior.[42] One strategy to enhance C–O bond cleavage in HDO reactions is the combination of MS and AS through a bifunctional mechanism.[36] In addition, the tuning of these active sites' ratio is essential to avoid extensive hydrogenolysis products. The catalytic performance of the as-received γ-Fe_2O_3, together with structural and acidic characterizations, demonstrated that the HDO reactional stream can lead to the generation of different active sites, directly impacting the activity, selectivity, and stability of the catalyst. Aiming for enhanced and selective C–O bond cleavage over the acetone HDO reaction, a series of thermal pre-treatments under reducing and oxidizing atmospheres were employed over the as-received γ-Fe_2O_3, as a strategy to vary the $Fe^{3+}/Fe^{2+}/Fe^0$ species' ratio. The

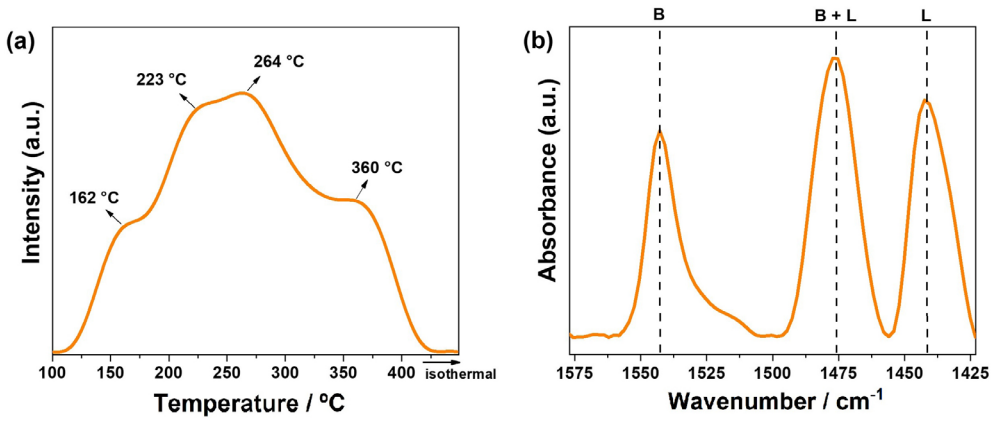

Figure 3. Acidic characterization over the as-received γ-Fe_2O_3 using (a) TPD-NH_3 and (b) Py-FTIR.

following catalytic tests were evaluated at 300 ºC, as a way to avoid extensive hydrogenolysis and fast deactivation over TOS, as previously observed for the as-received catalyst when submitted to reaction at 400 ºC (Figure 1c). It is worth noting that all pre-treated catalysts presented a significant decrease in the SSA when compared to the as-received γ-Fe_2O_3, from 98 $m^2\ g^{-1}$ to less than 10 $m^2\ g^{-1}$, respectively. This decrease can be attributed to sintering induced by the initial reduction of the oxidized to the metallic phase, as discussed later.

The performance of the reduced (Red 550) and reduced/oxidized (RedOxi 200, RedOxi 350, and RedOxi 500) catalysts over the acetone HDO as a function of TOS at 300 ºC are presented in Figure 4. The acetone conversion for the Red 550 (Figure 4a) started at 42.1%, increasing up to 55.2% after 3 h on stream. It presented an average DD of 94%, in which deoxygenated products accounted to C1 (4%), C2 (4%), C3E (43%), C3A (32%), C4 (2%), and C6 (9%), while oxygenated products accounted to IPA (5%) and C9O (1%). Products' distribution and DD remained quite stable along TOS, with the exception of C3E and C3A: C3E started representing 52.2% of the total products, decreasing to 36.4% after 3 h on stream; whereas C3A increased from 23 to 39%. Nevertheless, the total amount of C3 products remained around 75% during the entire TOS.

After oxidizing Red 550 at 200 ºC (RedOxi 200, Figure 4b) the acetone conversions decreased to around 35%; the products' distribution revealed that the catalyst suffered an induction period in the first hour on stream, resulting in similar selectivity to that observed for the Red 550 but with lower activity (at the end, 25% conversion). Initially, the DD was about 41.1% and its major products were C6 (21.8%), C9O (30.7%), C6O (15.9%), IPA (12.5%), and C9 (9.9%), which were mostly dependent on acid sites, associated with oxidized phases of iron. After the induction period (TOS > 1 h), the DD increased to 84.6% and the products' distribution was represented by C1 (2.6%), C2 (2.6%), C3E (51.2%), C3A (24.3%), IPA (14.3%), C6 (4.0%), and C9O (1%). The expressive modifications on the catalytic performance observed over TOS suggest that the evolution of different active sites occurred during the first hour on stream.

By oxidizing Red 550 at an intermediate temperature (RedOxi 350, Figure 4c), expressive modifications in the catalytic performance could be observed. Acetone conversions increased from 42.6 to 48.3% along the TOS, while the distribution of the products did not significantly

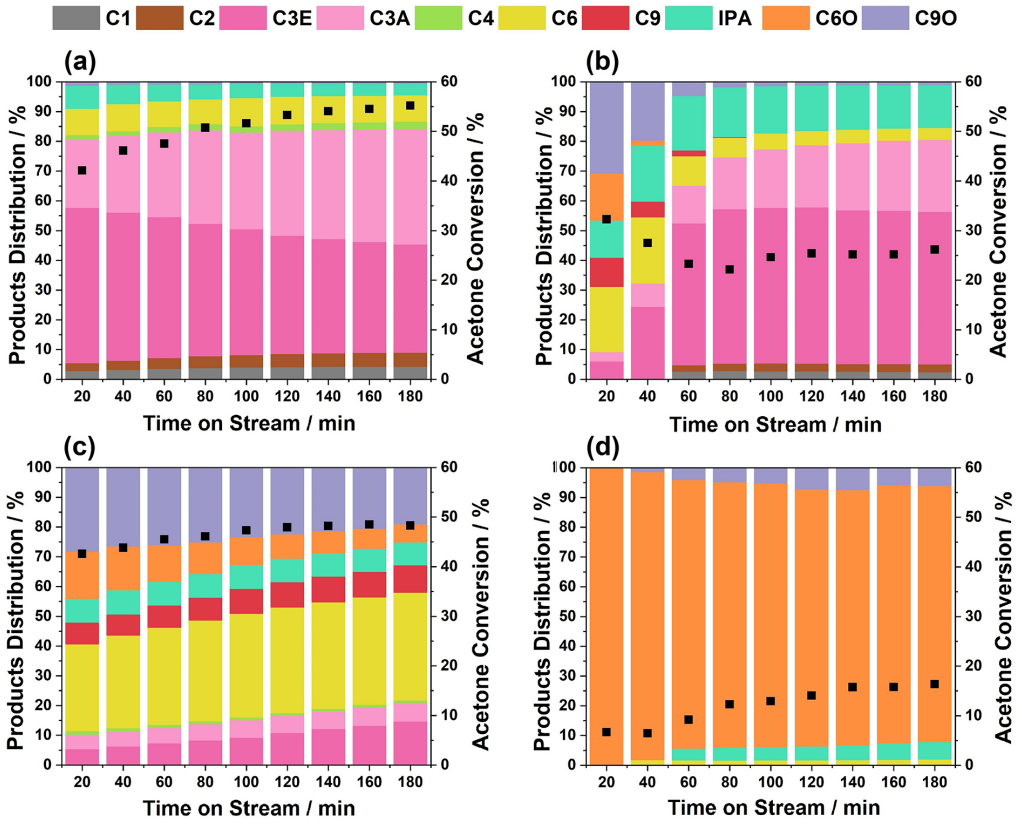

Figure 4. Product distribution (bars, left axis) and acetone conversions (squares, right axis) for the acetone HDO reaction as a function of TOS at 300 ºC: (a) Red 550, (b) RedOxi 200, (c) RedOxi 350, and (d) RedOxi 500. Feed: 3.6 mL min^{-1} acetone, 76 mL min^{-1} H_2, balance He. 100 mL min^{-1} total flow. WHSV = 0.94 $g_{acetone}\ [g_{iron}\ h]^{-1}$.

change up to 3 h on stream. The final distribution of products accounted for C3E (14.8%), C3A (6.2%), C4 (1.0%), C6 (36.2%), C9 (9.2%), IPA (7.7%), C6O (6.0%), and C9O (18.9%). As a consequence, an increase in the DD, from 48.0 to 67.4% could also be observed after 3 h on stream. It is also interesting to highlight that the distribution of the products at the beginning of the reaction for RedOxi 200 resembles RedOxi 350, suggesting the presence of similar active sites. Finally, a harsher oxidation was conducted over Red 550 (RedOxi 500, Figure 4d), leading to a decrease in activity, with acetone conversions ranging from 6.7 to 16.4%. The products' distribution was also modified, mainly associated with condensation products during the entire TOS (≥ 92%), suggesting the high availability of acid sites on the surface of the catalyst. Moreover, the catalytic performance of RedOxi 500 resembles the as-received γ-Fe_2O_3 catalyst (Figure 1b and Table 2). Table 3 summarizes the catalytic performance of this set of catalysts.

XRD measurements were conducted over the pre- and post-reaction catalysts to get insights into the structural modifications induced by the thermal pre-treatments and by the HDO reactional conditions (Figure 5 and Table S2, SI section). Pre-reaction Red 550 presented two reflections at 2θ = 44.7° and 65.3° (Figure 5a), attributed to the bcc metallic phase of iron, with a mean crystallite size of 77.5 nm. The exposure of the catalyst to the reactional stream for 3 h did not impact the final iron crystalline phase (Figure 5b) but led to a significant decrease in the crystalline domain (32.4 nm). For RedOxi 200, metallic iron was still the only observed crystalline phase (Figure 5a) but with smaller crystalline domains, 54.5 nm. Post-reaction RedOxi 200 (Figure 5b) did not present significant change in terms of crystalline phase, but the final mean crystalline domain was similar to the Red 550. These results indicated that the mild oxidation induced by the pre-treatment at 200 ºC forms an amorphous surface oxide layer that evolves under reaction conditions to a final state similar to the Red 550.

Oxidative pre-treatment at intermediate temperature, RedOxi 350, led to the partial oxidation of Red 550 (Figure 5a), resulting in a mixture of iron bcc, α-Fe_2O_3, and γ-Fe_2O_3/Fe_3O_4 crystalline phases. Post-reaction RedOxi 350 XRD pattern (Figure 5b) demonstrated that the reactional stream suppressed the α-Fe_2O_3 phase (Figure 5b). Finally, a harsher oxidation, RedOxi 500, led

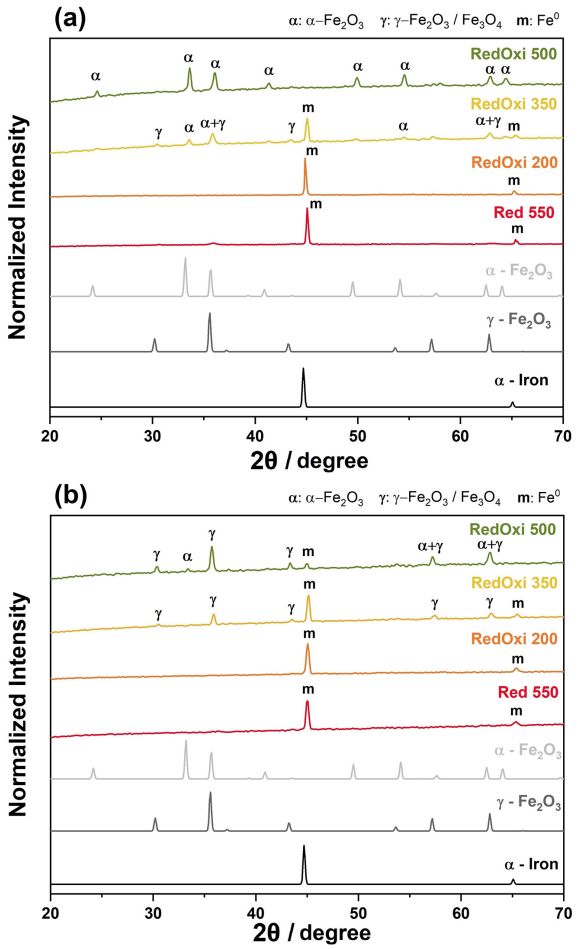

Figure 5. XRD measurements of the pre- (a) and post-reaction (b) Red 550, RedOxi 200, RedOxi 350, and RedOxi 500. The theoretical XRD pattern of α-Fe, α-Fe_2O_3 and γ-Fe_2O_3 are shown for comparison purposes.

Table 3. Initial (TOS = 20 min) and final (TOS = 180 min, within parenthesis) distribution of products, acetone conversions, and DD of Red 550, RedOxi 200, RedOxi 350, and RedOxi 500

Catalyst	Conversion / %	C1, C2, C4 / %	C3E/A / %	C6, C9 / %	IPA / %	C6O, C9O / %	DD / %
Red 550	42.1 (55.2)	7.0 (11.5)	75.3 (75.2)	8.8 (8.8)	7.7 (3.9)	1.1 (0.6)	91.1 (95.5)
RedOxi 200	32.3 (26.2)	0.0 (5.2)	9.3 (75.5)	21.8 (4.0)	12.4 (14.4)	46.5 (1.0)	41.0 (84.6)
RedOxi 350	42.6 (48.3)	1.2 (0.9)	10.3 (21.1)	36.5 (45.4)	8.0 (7.7)	44.0 (24.9)	48.0 (67.4)
RedOxi 500	6.7 (16.4)	0.0 (0.0)	0.0 (0.0)	0.0 (2.1)	0.0 (5.9)	100.0 (92.1)	0.0 (2.1)

DD: deoxygenation degree; IPA: isopropanol.

to the total oxidation of Red 550 forming the α-Fe_2O_3 phase (Figure 5a) but it was not stable under reaction conditions. The main final phase of RedOxi 500 was γ-Fe_2O_3/Fe_3O_4 with the co-existence of minor contributions of α-Fe_2O_3 and α-Fe. These results confirm that the α-Fe_2O_3 was not stable under the HDO reaction atmosphere, as was previously observed for the RedOxi 350 catalyst. Detailed information regarding the crystallite mean sizes of the different phases of the pre- and post-reaction catalysts is presented in Table S2 (SI section).

It was demonstrated that metallic and/or oxidized phases of iron can lead to different catalytic performances over the acetone HDO reaction at 300 ºC as a function of TOS (Figure 4). The main catalytic pathway observed for Red 550 was towards direct deoxygenation products (C3E and C3A) (about 75%), which can be mediated through oxygen vacancy (or oxophillic) sites or a bifunctional mechanism comprising metallic and acid sites. The presence of iron metallic sites was confirmed by XRD (Figure 5a). Deoxygenated C–C coupling products were also observed (9%), suggesting that a small fraction of AS was also available at the surface of the catalyst. It is worth noting the hydrogenation capability of the catalyst increased over TOS, favoring the formation of C3A over C3E (Figure 4a), which could be associated with the surface reconstruction under reactional stream. The slight increase (about 2%) in the formation of C–C bond cleavage products (i.e., C1, C2, and C4) over TOS also corroborates this hypothesis.

A mild oxidation of Red 550 (RedOxi 200) was not enough to induce the formation of a crystalline iron oxide phase (Figure 5a shows only the α-Fe phase). However, the formation of condensation products during the first hour on stream (Figure 4b) suggests the presence of a thin oxide layer, resulting in the availability of AS sites. This surface oxide was reduced under TOS due to the highly reducing atmosphere, leading to similar selectivity as Red 550 (Figure 4a).

An intermediate oxidation of Red 550 (RedOxi 350) led to the formation of a range of C–C coupling, hydrogenolysis, hydrogenation, and (hydro)deoxygenation products (Figure 4c), comprising different active sites and reaction pathways. XRD patterns of pre- and post-reaction RedOxi 350 confirmed the presence of metallic and oxidized phases of iron, however, the α-Fe_2O_3 phase was suppressed after being exposed to the reactional environment for 3 h, demonstrating that it was not stable. These results corroborate that the coexistence of metallic and oxidized phases of iron leads to active sites with different natures. Notably, the catalytic performance of RedOxi 350 resembles RedOxi 200 at the beginning of the reaction, suggesting that mild calcination led to similar active sites. However, by increasing the temperature, a crystalline oxide phase was formed on the surface of RedOxi 350, one more stable under reactional stream.

A harsher oxidation of Red 550 (RedOxi 500) resulted in a catalytic performance that resembles the as-received catalyst (Figure 1b), demonstrating the prevalence of AS and the formation of condensation products. XRD pattern of pre-reaction RedOxi 500 (Figure 5a) confirms, however, the presence of α-Fe_2O_3 phase. Comparing the pre- and post-reaction XRD patterns (Figure 5), the α-Fe_2O_3 phase was not stable and almost completely converted to γ-Fe_2O_3/Fe_3O_4 after 3 h on stream, similar to the as-received γ-Fe_2O_3 nanopowder catalyst. Interestingly, the reactional stream led to the formation of a minor crystalline metallic phase in RedOxi 500, but the distribution of the products suggests that these sites are not available or active.

Through the correlation of the obtained catalytic and structural data, it is possible to infer the nature of the surface of the catalyst and the present catalytic sites. The great selectivity towards C3 products shown by Red 550, in which the XRD analysis indicates the presence of only α-Fe crystalline domains, highlights the oxophilicity of metallic iron and the ability to promote the C–O cleavage. This mechanism may happen through either or both: the direct deoxygenation path (via reverse Mars van Krevelen, where the acetone would partially oxidize the surface of the iron) and the bifunctional mechanism, hydrogenating the carbonyl to alcohol, which would then be dehydrated to propylene by weak acid sites, as seen in Scheme 1. The oxophilic character of iron and its preference for C–O cleavage is well known in the literature, corroborating our findings. Hong *et al.*[48] obtained 90% selectivity towards BTX (aromatics: benzene, toluene, and xylene) in the *m*-cresol HDO using Pd/Fe_2O_3 catalysts, attributing the C–O bond adsorption to the oxophilic iron sites, while Pd promoted most of the H_2 activation. In turn, Marchenko *et al.*[30] observed that the oxophilic iron sites in Fe_xPt_{100-x} acted directly in the selective cleavage of aromatic C=O bond during acetophenone HDO.

The soft oxidation of Red 550 at 200 ºC (RedOxi 200) led to the formation of a thin shell of FeO_x over the metallic core, creating a heterogeneous surface consisting of available metallic and acid sites. This FeO_x layer was, however, unstable under HDO conditions once the product's distribution changed from a mixture of products (in agreement with the coexistence of different active sites) back to Red 550 related products, as seen in Figure 4b. Furthermore, pre- and post-reaction XRDs revealed α-Fe as the only crystalline phase. By increasing the pre-treatament oxidation temperature to

350 ºC (RedOxi 350), a thick crystalline oxide layer was formed, that was partially stable under reaction conditions. The heterogeneity of the surface was evident by the distribution of the products, related to MS (C3E/A, C1, C2, C4, and IPA) or to AS (C6O and C9O) and by the presence of deoxygenated C–C coupling products (C6 and C9), which require the availability of both sites with enough proximity to work cooperatively. The XRD analysis confirmed the coexistence of different iron phases, and, therefore, catalytic sites. Lastly, a harsher oxidation condition (RedOxi 500) led to the total oxidation of iron, which was partially reduced under reaction, however, the MS were mostly unavailable.

Modifications on a Co_3O_4 nanopowder catalyst using sequential reducing/oxidizing pre-treatments and similar acetone HDO reaction conditions to this work were reported before and a comparison can be made.[3] The activity of reduced γ-Fe_2O_3 (103 $mmol_{acetone}\ g_{cat}^{-1}\ h^{-1}$) was about 35% lower than reduced Co_3O_4 (157 $mmol_{acetone}\ g_{cat}^{-1}\ h^{-1}$). However, the reduced Co_3O_4 catalyst led to a C–O/C–C bond cleavage ratio of 0.39 against 11.9 for the reduced γ-Fe_2O_3, highlighting the high selectivity towards C–C bond cleavage products for cobalt, and C–O bond cleavage products for iron. The significant differences in selectivity can be correlated with the intrinsic nature of the metals: cobalt led to more active catalysts, but due to the enhanced hydrogenation capability compared to iron, it majorly mediated C–C bond cleavage products (62%). Additionally, in both systems, the intermediate oxidation pre-treatment (200 ºC for Co_3O_4 and 350 ºC for γ-Fe_2O_3), resulted in products associated with multisite surfaces. It demonstrates that tuning the ratio between different species of bulk earth-abundant metals is a promising way of designing catalysts with enhanced selectivity towards HDO reactions.

Conclusions

The catalytic performance of γ-Fe_2O_3 nanopowder was evaluated in the acetone HDO reaction as a function of temperature and TOS. At lower temperatures (≤ 300 ºC), the formation of condensation products was favored, which was attributed to the presence of AS on the surface of the catalyst. Higher temperatures, i.e., 400 ºC, led to extensive C–O and C–C bond cleavage products followed by a quick deactivation, demonstrating that the reactional stream induced the formation of active sites with metallic behavior prone to deactivation. Structural analysis of the post-reaction catalyst confirmed the formation of iron carbidic phases, responsible for the enhancement in the hydrogenation capability of the catalyst. Reduction/oxidation pre-treatments over the γ-Fe_2O_3 nanopowder led to pronounced and positive modifications in the catalytic performance over the acetone HDO reaction at 300 ºC. XRD analyses of pre- and post-reaction catalysts provided insights into structural modifications induced by thermal treatments and the reactional stream. It was demonstrated that by rationalizing $Fe^{3+}/Fe^{2+}/Fe^0$ sites, it was possible to favor different reaction pathways: (*i*) C–C coupling products, i.e., condensation products, mediated through AS; (*ii*) direct C–O bond cleavage products, mediated through OVS and/or bifunctional mechanism comprising MS and AS; and (*iii*) cascade C–C coupling and C–O cleavage products, mediated through a multisite surface. This study demonstrated that the coexistence of metallic and oxidized phases of iron impacted the catalytic performance, highlighting the importance of tuning the catalytic site ratios for active, selective, and stable catalysts for HDO reactions.

Supplementary Information

Supplementary information (Figure S1 and Tables S1-S2) is available free of charge at http://jbcs.sbq.org.br as PDF file.

Acknowledgments

This work was funded in part by Fundação de Amparo à Pesquisa do Estado de São Paulo (FAPESP 2018/01258-5, 2020/12986-1, 2022/09325-9), Conselho Nacional de Desenvolvimento Científico e Tecnológico (CNPq 140849/2020-3, 311226/2022-1, 409401/2023-4), and Coordenação de Aperfeiçoamento de Pessoal de Nível Superior (CAPES finance code 001). We are grateful to Davi dos Santos Leite for the fruitful discussions that contribute to our work.

References

1. Ethiraj, J.; Wagh, D.; Manyar, H.; *Energy Fuels* **2022**, *36*, 1189. [Crossref]
2. Michailof, C. M.; Kalogiannis, K. G.; Sfetsas, T.; Patiaka, D. T.; Lappas, A. A.; *Wiley Interdiscip. Rev.: Energy Environ.* **2016**, *5*, 614. [Crossref]
3. Leite, D. S.; Strapasson, G. B.; Zanchet, D.; *Mol. Catal.* **2022**, *530*, 112623. [Crossref]
4. Gollakota, A. R. K.; Shu, C. M.; Sarangi, P. K.; Shadangi, K. P.; Rakshit, S.; Kennedy, J. F.; Gupta, V. K.; Sharma, M.; *Renewable Sustainable Energy Rev.* **2023**, *187*, 113700. [Crossref]
5. Haynes, W. M.; *Handbook of Chemistry and Physics*, 95th ed.; CRC Press: Boca Raton, US, 2014.
6. Inorganic Crystal Structure Database, https://icsd.fiz-karlsruhe.de/, accessed in June 2024.

7. Dilanian, R. A.; Izumi, F.; *Visualization for Electronic and Structural Analysis* (*VESTA)*, version 3.5.8; National Museum of Nature and Science, Japan, 2006.
8. Honkala, K.; Hellman, A.; Remediakis, I. N.; Logadottir, A.; Carlsson, A.; Dahl, S.; Christensen, C. H.; Nørskov, J. K.; *Science* **2005**, *307*, 555. [Crossref]
9. Iglesia, E.; Reyes, S. C.; Madon, R. J.; Soled, S. L.; *Selectivity Control and Catalyst Design in the Fischer-Tropsch Synthesis: Sites, Pellets, and Reactors*, vol. 39, 1st ed.; Academic Press: Cambridge, US, 1993. [Crossref]
10. van der Laan, G. P.; Beenackers, A. A. C. M.; *Catal. Rev.: Sci. Eng.* **1999**, *41*, 255. [Crossref]
11. Guo, X.; Fang, G.; Li, G.; Ma, H.; Fan, H.; Yu, L.; Ma, C.; Wu, X.; Deng, D.; Wei, M.; Tan, D.; Si, R.; Zhang, S.; Li, J.; Sun, L.; Tang, Z.; Pan, X.; Bao, X.; *Science* **2014**, *344*, 616. [Crossref]
12. Brandenberger, S.; Kröcher, O.; Tissler, A.; Althoff, R.; *Catal. Rev.* **2008**, *4*, 492. [Crossref]
13. Hong, Y.; Hensley, A.; McEwen, J. S.; Wang, Y.; *Catal. Lett.* **2016**, *146*, 1621. [Crossref]
14. Li, J.; Zhang, J.; Wang, S.; Xu, G.; Wang, H.; Vlachos, D. G.; *ACS Catal.* **2019**, *9*, 1564. [Crossref]
15. Liu, T.; Tian, Z.; Zhang, W.; Luo, B.; Lei, L.; Wang, C.; Liu, J.; Shu, R.; Chen, Y.; *Fuel* **2023**, *339*, 126916. [Crossref]
16. Olcese, R.; Bettahar, M. M.; Malaman, B.; Ghanbaja, J.; Tibavizco, L.; Petitjean, D.; Dufour, A.; *Appl. Catal., B* **2013**, *129*, 528. [Crossref]
17. Yang, J.; Li, S.; Zhang, L.; Liu, X.; Wang, J.; Pan, X.; Li, N.; Wang, A.; Cong, Y.; Wang, X.; Zhang, T.; *Appl. Catal., B* **2017**, *201*, 266. [Crossref]
18. Zanuttini, M. S.; Gross, M.; Marchetti, G.; Querini, C.; *Appl. Catal., A* **2019**, *587*, 117217. [Crossref]
19. Li, C.; Nakagawa, Y.; Tamura, M.; Nakayama, A.; Tomishige, K.; *ACS Catal.* **2020**, *10*, 14624. [Crossref]
20. Li, C.; Nakagawa, Y.; Yabushita, M.; Nakayama, A.; Tomishige, K.; *ACS Catal.* **2021**, *11*, 12794. [Crossref]
21. Chen, Q.; Cai, C.; Zhang, X.; Zhang, Q.; Chen, L.; Li, Y.; Wang, C.; Ma, L.; *ACS Sustainable Chem. Eng.* **2020**, *8*, 9335. [Crossref]
22. Rizescu, C.; Sun, C.; Popescu, I.; Urdă, A.; Da Costa, P.; Marcu, I. C.; *Catal. Today* **2021**, *366*, 235. [Crossref]
23. Li, J.; Liu, J. L.; Liu, H. Y.; Xu, G. Y.; Zhang, J. J.; Liu, J. X.; Zhou, G. L.; Li, Q.; Xu, Z. H.; Fu, Y.; *ChemSusChem* **2017**, *10*, 1436. [Crossref]
24. Yang, Y.; Tan, M.; Garcia, A.; Zhang, Z.; Lin, J.; Wan, S.; McEwen, J. S.; Wang, S.; Wang, Y.; *ACS Catal.* **2020**, *10*, 7884. [Crossref]
25. Zhang, J.; Sudduth, B.; Sun, J.; Kovarik, L.; Engelhard, M. H.; Wang, Y.; *ChemSusChem* **2021**, *14*, 4546. [Crossref]
26. Lin, S. H.; Hetaba, W.; Chaudret, B.; Leitner, W.; Bordet, A.; *Adv. Energy Mater.* **2022**, *12*, 2201783. [Crossref]
27. Wang, S.; Xu, D.; Chen, Y.; Zhou, S.; Zhu, D.; Wen, X.; Yang, Y.; Li, Y.; *Catal. Sci. Technol.* **2020**, *10*, 3015. [Crossref]
28. Ji, N.; Wang, X.; Weidenthaler, C.; Spliethoff, B.; Rinaldi, R.; *ChemCatChem* **2015**, *7*, 960. [Crossref]
29. Dou, X.; Li, W.; Zhu, C.; Jiang, X.; *Appl. Catal., B* **2021**, *287*, 119975. [Crossref]
30. Marchenko, N.; Lacroix, L. M.; Ratel-Ramond, N.; Leitner, W.; Bordet, A.; Tricard, S.; *ACS Appl. Nano Mater.* **2023**, *6*, 20231. [Crossref]
31. Zhang, J.; Sun, J.; Kovarik, L.; Engelhard, M. H.; Du, L.; Sudduth, B.; Li, H.; Wang, Y.; Wang, Y.; *Chem. Sci.* **2020**, *11*, 5874. [Crossref]
32. Prasomsri, T.; Nimmanwudipong, T.; Román-Leshkov, Y.; *Energy Environ. Sci.* **2013**, *6*, 1732. [Crossref]
33. Mars, P.; Van Krevelen, D. W.; *Chem. Eng. Sci.* **1954**, *3*, 41. [Crossref]
34. Strapasson, G. B.; Sousa, L. S.; Báfero, G. B.; Leite, D. S.; Moreno, B. D.; Rodella, C. B.; Zanchet, D.; *Appl. Catal., B* **2023**, *335*, 122863. [Crossref]
35. Báfero, G. B.; Strapasson, G. B.; Leite, D. S.; Zanchet, D.; *ChemCatChem* **2023**, *15*, e202300663. [Crossref]
36. Wang, J.; Jabbour, M.; Abdelouahed, L.; Mezghich, S.; Estel, L.; Thomas, K.; Taouk, B.; *Can. J. Chem. Eng.* **2021**, *99*, 1082. [Crossref]
37. Wagloehner, S.; Baer, J. N.; Kureti, S.; *Appl. Catal., B* **2014**, *147*, 1000. [Crossref]
38. Zaki, M. I.; Hasan, M. A.; Al-Sagheer, F. A.; Pasupulety, L.; *Colloids Surf., A* **2001**, *190*, 261. [Crossref]
39. Manjunathan, P.; Shanbhag, G. V. In *Tin Oxide Materials*; Orlandi, M. O., ed.; Elsevier: Amsterdam, 2020, ch. 18.
40. Manjunathan, P.; Prasanna, V.; Shanbhag, G. V.; *Sci. Rep.* **2021**, *11*, 15718. [Crossref]
41. Tamura, M.; Shimizu, K. I.; Satsuma, A.; *Appl. Catal., A* **2012**, *433*, 135. [Crossref]
42. Kirchner, J.; Anolleck, J. K.; Lösch, H.; Kureti, S.; *Appl. Catal., B* **2018**, *223*, 47. [Crossref]
43. Liu, Y.; Murthy, P. R.; Zhang, X.; Wang, H.; Shi, C.; *New J. Chem.* **2021**, *45*, 22444. [Crossref]
44. Zieliński, J.; Zglinicka, I.; Znak, L.; Kaszkur, Z.; *Appl. Catal., A* **2010**, *381*, 191. [Crossref]
45. Corma, A.; *Chem. Rev.* **1995**, *95*, 559. [Crossref]
46. Kayo, A.; Yamaguchi, T.; Tanabe, K.; *J. Catal.* **1983**, *83*, 99. [Crossref]
47. Emeis, C. A.; *J. Catal.* **1993**, *141*, 347. [Crossref]
48. Hong, Y.; Zhang, H.; Sun, J.; Ayman, K. M.; Hensley, A. J. R.; Gu, M.; Engelhard, M. H.; McEwen, J. S.; Wang, Y.; *ACS Catal.* **2014**, *4*, 3335. [Crossref]

Submitted: February 9, 2024
Published online: July 17, 2024